Moisture transport axes and their relation to atmospheric rivers and warm moist intrusions

C. Spensberger[1], K. Konstali[1], T. Spengler[1]

[1]Geophysical Institute, University of Bergen, and Bjerknes Centre for Climate Research, Bergen, Norway

Key Points:

- Moisture transport axes identify moisture pathways in all climate zones, conceptually unifying atmospheric rivers and warm moist intrusions
- The definition of moisture transport axes is based on the elongated structure of moisture transport filaments
- Robust detection across current climate zones suggests a robust definition across changing climates

Corresponding author: Clemens Spensberger, clemens.spensberger@uib.no

Abstract

The water vapor transport in the extratropics is mainly organized in narrow elongated filaments. These filaments are referred to with a variety of names depending on the contexts. When making landfall on a coastline, they are generally referred to as atmospheric rivers; when occurring at high latitudes, many authors regard them as warm moist intrusions; when occurring along a cold front and near a cyclone core, the most commonly used term is warm conveyor belt. Here, we propose an algorithm that detects these various lines of moisture transport in instantaneous maps of the vertically integrated water vapor transport. The detection algorithm extracts well-defined maxima in the water vapor transport and connects them to lines that we refer to as moisture transport axes. By only requiring a well-defined maximum in the vapor transport, we avoid imposing a threshold in the absolute magnitude of this transport (or the total column water vapor). Consequently, the algorithm is able to pick up moisture transport axes at all latitudes without requiring region-specific tuning or normalization. We demonstrate that the algorithm can detect both atmospheric rivers and warm moist intrusions. Atmospheric rivers sometimes consist of several distinct moisture transport axes, indicating the merging of several moisture filaments into one atmospheric river. Finally, we showcase the synoptic situations and precipitation patterns associated with the occurrence of the identified moisture transport axes in example regions in the low, mid, and high latitudes.

Plain Language Summary

The transport of moisture from warmer and moister regions towards colder and drier regions mainly occurs in brief and narrow bursts that can lead to extreme amounts of precipitation upon landfall. In the mid-latitudes, such bursts are generally referred to as *atmospheric rivers*, whereas in the Arctic they are often referred to as *warm moist intrusions*. We introduce a new and more general definition of what constitutes such bursts of moisture transport, which is based primarily on their narrow, elongated structure. Using this more general definition, we show that similar bursts in moisture transport occur frequently across all climate zones, including polar and tropical regions. In the Tropics, for example, we identify seasonal variations in moisture transport, such as those associated with the Asian monsoon.

1 Introduction

Throughout the mid-latitudes, the bulk of the moisture transport occurs in narrow filaments (Newell et al., 1992; Zhu & Newell, 1994, 1998; Sodemann & Stohl, 2013; Dacre et al., 2015) that received much attention under the label *atmospheric river* (Zhu & Newell, 1994; Rutz et al., 2019; Lora et al., 2020). Landfalling atmospheric rivers are thus key contributors to the hydrological cycle and can produce intense precipitation events that lead to flooding (Zhu & Newell, 1994; Sodemann & Stohl, 2013). A recent intercomparison, however, highlights that the definition of atmospheric rivers diverges widely (ARTMIP; Rutz et al., 2019), where the choice of the diagnostic variable, threshold, and normalization method remains a subjective choice that often depends on the study region. To devise a detection algorithm that is more generally applicable across different regions, we introduce an alternative approach focusing on the structure of moisture filaments rather than their intensity.

Moisture filaments, very much like atmospheric rivers, also occur at higher latitudes (Sorteberg & Walsh, 2008; Woods & Caballero, 2016; Papritz et al., 2022). In the Arctic, such features would typically be called *warm moist intrusions* (Woods & Caballero, 2016; Papritz et al., 2022). Gorodetskaya et al. (2014), however, apply the same concept and label moisture filaments making landfall in Antarctica as *atmospheric rivers*. Although using the same label, atmospheric rivers in polar regions either require region-specific tuning or normalization of the input fields to accommodate for the much lower

absolute moisture content compared to, for example, California (cf. differences in polar and mid-latitude-focused algorithms in ARTMIP; Rutz et al., 2019).

Our detection algorithm instead targets the structure of moisture filaments. We take this approach from an upper tropospheric jet detection algorithm (Spensberger et al., 2017; Spensberger & Spengler, 2020). Jet axes are defined as lines of maximum winds at the dynamical tropopause. We apply this approach to the vertically integrated water vapor transport (IVT) and trace lines of maximum moisture transport. We do not require a minimum threshold of IVT, but rather that the maximum in the moisture transport is well-defined.

This approach is similar to atmospheric river detection algorithms that include transport axes to define the start, end, or length of an atmospheric river. Mundhenk et al. (2016) derive such an axis a-posteriori from the outline of a 2-dimensional atmospheric river object, whereas Wick et al. (2013) does so by applying techniques from image processing. Similar to our approach, Lavers et al. (2012) and Griffith et al. (2020) define the axis by the maximum transport, but require a target region and consider only lines of maxima that continuously extend westward from that region. In contrast to previous approaches, our algorithm is directly and only based on the structure of the IVT vector field and identifies maxima in the IVT, irrespective of its orientation. Geometric features like start point, end point, and length are thus straightforward and unambiguously defined.

There are several further advantages of considering moisture filaments as a one-dimensional rather than two-dimensional feature. First, as we will show, an atmospheric river outline can contain several distinct maxima in the moisture transport where these maxima can even be oriented in nearly opposing directions. Finally, moisture transport axes visually highlight the direction of the moisture transport, for example relative to the orientation of a coastline, which is essential to assess orographic precipitation (Griffith et al., 2020).

2 Data and detection method

We base our study on 3-hourly ERA5 reanalysis at 0.5° resolution for the period 1979-2020 (Hersbach et al., 2020). We follow Spensberger et al. (2017) and Spensberger and Spengler (2020) and filter the IVT components to T84 resolution as the detection algorithm is somewhat sensitive to grid point noise. This resolution is fine enough to retain all synoptic scale and many mesoscale structures (cf., Spensberger et al., 2017, and the case study snapshots herein; Figs. 2; 6a,b; 7a,b; 8a,b; and A1 in the appendix).

The detection identifies lines of maximum IVT (method illustrated in Fig. 1), analogous to the jet axis detection tracing lines of maximum wind (Spensberger et al., 2017). The algorithm identifies well-defined maxima in IVT in cross sections normal to the IVT direction (e.g., the sections in Fig. 1). In practice, we find locations where the "shear" σ in IVT,

$$\sigma_{\mathrm{IVT}} = \frac{\partial \mathrm{IVT}}{\partial n} = 0 \quad , \tag{1}$$

by checking for all pairs of neighboring grid points whether σ_{IVT} has changed sign. Here, n is the direction perpendicular to the direction of the local water vapor transport. This procedure is analogous to the jet axis detection which identifies the location of the wind maximum by the zero-shear line, the line marking the transition from cyclonic to anticyclonic shear. We pinpoint the exact location of the $\sigma_{\mathrm{IVT}} = 0$-line by linear interpolation between identified pairs of neighboring grid points.

In the second step, we filter out IVT minima and weak IVT maxima by requiring

$$|\mathrm{IVT}| \cdot \frac{\partial \sigma_{\mathrm{IVT}}}{\partial n} \leq K_{\mathrm{IVT}} \quad , \tag{2}$$

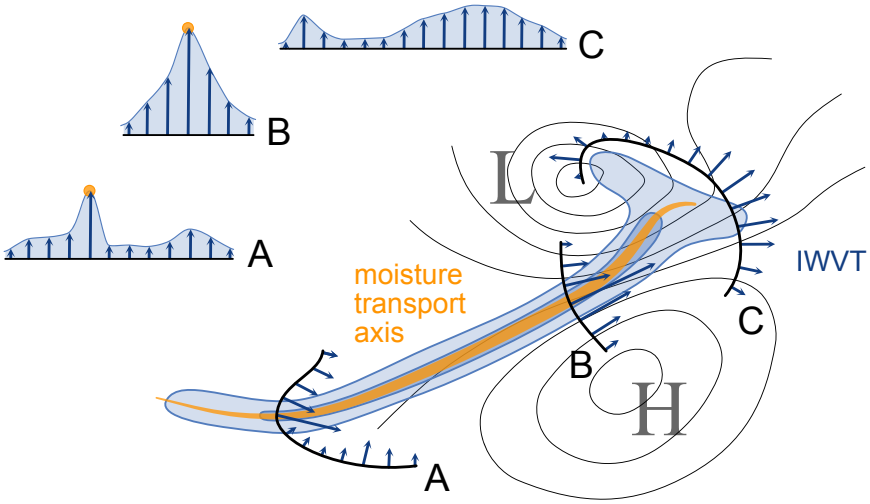

Figure 1. Illustration of the detection method. Blue contours and vectors show the magnitude and direction of the vertically integrated water vapor transport (IVT). The black lines marked A, B and C are cross sections perpendicular to the local IVT direction. Well-defined maxima in the local IVT along the sections are marked by yellow circles in A and B; these well-defined maxima are then connected to form the yellow moisture transport axis line. Black contours indicate isobars, and the labels L and H mark a cyclone and an anticyclone, respectively.

where $K_{\mathrm{IVT}} = -4.06 \cdot 10^{-7}\,\mathrm{kg^2 s^{-2} m^{-4}}$, derived from ERA5 by following the suggestion of Spensberger et al. (2017) and using the 12.5-percentile of $|\mathrm{IVT}| \cdot \frac{\partial \sigma_{\mathrm{IVT}}}{\partial n}$. Minima in IVT do not fulfill this criterion, because there $\frac{\sigma_{\mathrm{IVT}}}{\partial n} > 0$. Well-defined maxima are thus defined by a combination of absolute magnitude ($|\mathrm{IVT}|$) and the sharpness of the IVT maximum ($\frac{\partial \sigma_{\mathrm{IVT}}}{\partial n}$). Small-amplitude maxima can become part of a moisture transport if the associated peak in IVT is sharp enough (yellow dots in the cross sections A and B in Fig. 1).

In a third step, we connect all remaining points marking well-defined IVT maxima into lines using a maximum distance of 1.5 grid points between two successive points along a line (further details on this step in Spensberger et al., 2017). In the fourth and final step, we require a minimum length of 2000 km for such a line to become a moisture transport axes (yellow line in Fig. 1). This minimum length is in line with typical geometry constraints used for detecting atmospheric rivers (Rutz et al., 2019).

3 Case studies from low, mid, and high latitudes

To illustrate the performance of the detection algorithm, we first showcase selected occurrences of moisture transport axes (yellow lines in Fig. 2). Three of the four cases in Fig. 2 are based on previous studies of atmospheric rivers. The North Pacific and South Indian Ocean cases are discussed in Lora et al. (2020) (our Fig. 2a-d). The North Atlantic case (Fig. 2e,f) is discussed in Azad and Sorteberg (2017) and yielded one of the highest daily precipitation totals on record in Bergen on the west coast of Norway. These cases also include examples of high-latitude moisture transport axes, such as the one touching the Antarctic coastline south of Africa (Fig. 2d) and the one close to Novaya Zemlya (Fig. 2f). The fourth case highlights a moisture transport axis from the Sahel region across the Sahara towards the Mediterranean (Fig. 2g,h). This moisture transport axis is as-

sociated with scattered patches of precipitation exceeding 1 mm/h over the Sahara desert (magenta contours in Fig. 2g,h).

At all latitudes, the showcased moisture transport axes clearly trace maxima in the moisture transport (right column of Fig. 2), despite the large variation in the absolute magnitude of the IVT along the various axes and across the different climate zones. Many axes extend beyond the outermost highlighted IVT contour at $250\,\mathrm{kg\,s^{-1}\,m^{-1}}$ and some trace IVT maxima beyond the saturation of the color scale at $1150\,\mathrm{kg\,s^{-1}\,m^{-1}}$.

For mid-latitude moisture transport axes, the cases suggest a qualitatively good correspondence to typical atmospheric river detections. More specifically, our moisture transport axes correspond well to the majority consensus detections for the cases discussed in Lora et al. (2020, their Fig. 4c,g). In contrast to atmospheric rivers, however, moisture transport axes highlight the diffluent moisture transport close to the occlusion point of a cyclone (e.g., Fig. 2b). From the occlusion point, one branch of moisture transport typically spirals cyclonically towards the cyclone core, while another branch follows the warm front away from the cyclone core. The dominant branch varies from cyclone to cyclone (towards cyclone in Fig. 2b, away in Fig. 2d, both variants evident in Fig. 2f).

Beyond the mid-latitudes, moisture transport axes highlight moisture transport that would not generally be considered an atmospheric river and that would typically not be picked up by commonly used atmospheric river detection schemes. For example, the moisture transport axes pick up a moisture filament associated with only moderate IVT close to Novaya Zemlya (Fig. 2e,f). Moisture transport axes also pick up the cyclonic and nearly circular moisture transport around tropical cyclones (e.g., close to the North American east coast in Fig. 2f). Further, the moisture transport axes trace an expulsion of Tropical moisture into the much drier subtropics (Fig. 2h).

4 Climatology of moisture transport axes

Climatologically, the occurrence of moisture transport axes in the mid-latitudes follows the storm tracks (Fig. 3). This is particularly true for the winter hemisphere (Fig. 3a,c). During winter, the occurrence of moisture transport axes is closely related to the IVT climatology (gray contours in Fig. 3), whereas during summer and autumn, moisture transport axes occur frequently over the continents downstream of a storm track despite comparatively small climatological IVT.

In the Subtropics and Tropics, the occurrence of moisture transport axes is confined to some specific regions (Fig. 3). Moisture transport axes frequently occur along the Intertropical Convergence Zone (ITCZ) year-round. In addition, the monsoon circulation is frequently associated with moisture transport axes, for example the Indian monsoon (Fig. 3c) as well as the Somali Jet (Moisture transport in the Somali Jet discussed in detail in Viste & Sorteberg, 2013). The climatology of moisture transport axes also highlights the moisture transport along low-level jets steered by orography. This effect is apparent year-round along the South American low-level jet on the eastern side of the Andes (Montini et al., 2019), but also, with some seasonal variation, along the straits through the Maritime continent.

In comparison with the low and mid-latitudes, relatively few moisture transport axes occur in subpolar and polar regions (Fig. 3). Nevertheless, the 5%-frequency of occurrence isoline extends beyond 70°N in the North Atlantic during winter (Fig. 3a) and covers most of the ice-free Arctic Ocean during summer (Fig. 3c). Similarly, in the North Pacific, the Aleutian Islands have a moisture transport axis nearby for more than 5% of the time winter time steps. In the Southern Hemisphere, the 5%-isoline remains near the Antarctic coastline during all seasons and extends furthest poleward upstream of the Antarctic peninsula in the South Pacific sector.

In synthesis, the case studies and climatologies give a strong indication that our definition of moisture transport axes is able to detect moisture filaments across all climate zones. The detections appears to align well with the concept of atmospheric rivers in the mid-latitudes (a more stringent comparison follows in sec. 6), but also capture synoptically meaningful events in the Tropics, Subtropics, and polar regions.

5 Normalized detections

The frequent detection of moisture transport axes at low latitudes indicates that also many less impactful events, such as seasonal or even stationary features of the circulation, are picked up. For some applications, however, it might be desirable to limit detections to the most pronounced moisture filaments at low latitudes. In the following, we explore the normalization of the IVT input fields to the detection to achieve more selective detections at low latitudes.

For this analysis, we normalized the IVT by the annual and zonal mean total column water vapor $\overline{\mathrm{IWV}}$ (red lines in Fig. 2 show resulting detections, climatology in Fig. 4). Given that the non-normalized detections appear optimal around the western boundary currents, we aim to keep detections in these regions unchanged by the normalization. We achieve this by defining the normalized IVT_n by

$$\mathrm{IVT}_n = \mathrm{IVT}\frac{\overline{\mathrm{IWV}}(40°\mathrm{N/S})}{\max(\overline{\mathrm{IWV}}_{\mathrm{min}}, \overline{\mathrm{IWV}})}$$

and using IVT_n instead of IVT as input to the detection algorithm, while keeping the K_{IVT}-threshold unchanged. The annual zonal mean $\overline{\mathrm{IWV}}(40°\mathrm{N/S}) \approx 18\,\mathrm{kg\,m^{-2}}$ and we set a minimum $\overline{\mathrm{IWV}}_{\mathrm{min}} = 3\,\mathrm{kg\,m^{-2}}$ to avoid spurious detections over the extremely dry Antarctic continent. We considered alternative normalizations by the (zonally asymmetric) annual mean IWV as well as the seasonal mean IWV, but the results are qualitatively very similar (not shown).

In the case studies, the most prominent moisture filaments are detected both with and without normalization (compare red and yellow lines in Fig. 2). Nevertheless, there are clearly more (fewer) detections of transport axes at high (low) latitudes with the normalized detections. Analogously, normalized transport axes trace the moisture filament over longer (shorter) distances in the Arctic (Subtropics and Tropics).

Climatologically, most Tropical and Subtropical detections vanish with normalization (Fig. 4). The remaining moisture transport axes are associated with the South American low-level jet or with the Somali Jet and Indian Monsoon during the monsoon season (Fig. 4c). For the remainder of the Subtropics and Tropics, detections are limited to the most pronounced moisture filaments, which generally occur at less than 5% of the time steps for all seasons.

At the same time, more moisture transport axes are detected in polar regions. With normalization, the 5%-isoline touches the Antarctic continent year-round (Fig. 4). Similarly, in the North Atlantic, the detections during winter around 70° increase by around a factor of three, from approx. 5% to approx. 15% frequency of occurrence. Thus, with normalization, the occurrence of moisture transport axes becomes an event of everyday weather both in the Arctic and along the Antarctic coastline, capturing many less impactful moisture filaments.

6 Relation to atmospheric rivers

The climatologies of normalized and non-normalized moisture transport axes resemble the mean and median detection frequencies in the ARTMIP catalog (compare our Figs. 3 & 4 with Fig. 1a,b of Lora et al., 2020). The most obvious difference between

both the mean and median detections in ARTMIP as well as between our normalized and non-normalized detections is the frequency of detection in the Subtropics and Tropics. We observe a significant number of detections at low latitudes in both the ARTMIP mean and our non-normalized detections. However, in our climatologies of normalized moisture transport axes, we generally find more frequent detections over land and in the Arctic compared to most schemes in ARTMIP.

To corroborate the qualitatively good correspondence between moisture transport axes and atmospheric rivers documented by the case studies and climatologies, we supplement these analyses first by a quantitative comparison of the properties of moisture transport axes with different commonly used criteria to identify atmospheric rivers, and second by a composite analysis of moisture transport axes making landfall in Northern California.

Without normalization, the distribution across latitude is clearly bimodal with one narrow peak around 10° latitude as well as a wider peak centered around 45° latitude (Fig. 5a-d). The minimum in frequency of detections occurs around 20° latitude, a latitude considerably lower than the cutoff at 30°N/S used in some atmospheric river detection algorithms. These algorithms thus disregard moisture transport that seems more closely related to the extratropics than to the Tropics. With normalization, the bimodal distribution vanishes along with the low-latitude peak in detections and the extratropical peak shifts poleward (histogram on top of Fig. 5). Consequently, only 12% of the normalized moisture transport axes occur equatorward of 30°N/S, compared to 43% for the non-normalized detections.

The bimodality in latitude for the non-normalized detections is reflected in a slight bimodality also in IWV (Fig. 5a). Tropical moisture transport axes are associated with distinctly more IWV than extratropical moisture transport axes, with only a small overlap in the distributions around $45\,\mathrm{kg\,m^{-2}}$. The most frequent IWV in extratropical axes is approximately $20\,\mathrm{kg\,m^{-2}}$ and around 20% of the moisture transport axes are below this value that is sometimes used as a threshold.

Note that the histogram is based on all points along all moisture transport axes rather than the axes' peak intensity. The statistic thus implies that 20% of the combined length of all moisture transport axes is below the $20\,\mathrm{kg\,m^{-2}}$ threshold. With normalization, this statistic increases to 45%, i.e. 45% of the combined length of all normalized moisture transport axes extends beyond $20\,\mathrm{kg\,m^{-2}}$. The most frequent value IWV for the normalized axes is between 12 and $15\,\mathrm{kg\,m^{-2}}$ (histogram to the left of Fig. 5a).

Most detection algorithms for atmospheric rivers use IVT as one of their criteria to define the feature. Typical thresholds used are 250, 500 and $700\,\mathrm{kg\,s^{-1}\,m^{-1}}$ (Rutz et al., 2019; Lora et al., 2020). In comparison, the most common value IVT along moisture transport axes is around $350\,\mathrm{kg\,s^{-1}\,m^{-1}}$ (Fig. 5b). Interestingly, the most common value is largely independent of latitude (Fig. 5b). In particular, typical tropical and extratropical moisture axes are associated with similar IVT. The strongest IVT, beyond 700-$800\,\mathrm{kg\,s^{-1}\,m^{-1}}$, does however mostly occur around 45° latitude. Consequently, the vast majority (89%) of the non-normalized transport axes exceed the $250\,\mathrm{kg\,s^{-1}\,m^{-1}}$-threshold. At the same time, most of the axes are also located below the $500\,\mathrm{kg\,s^{-1}\,m^{-1}}$ and $700\,\mathrm{kg\,s^{-1}\,m^{-1}}$-thresholds (66 and 88%, respectively).

Instead of using a cut-off latitude, some definitions of atmospheric rivers rely on a threshold for the poleward and/or eastward component of the IVT (Rutz et al., 2019; Lora et al., 2020). The eastward component of the IVT also exhibits a bimodal distribution with a local minimum between the westerly and easterly modes at $0\,\mathrm{kg\,s^{-1}\,m^{-1}}$ (Fig. 5c). This bimodality maps reasonably well onto the bimodality in latitude, with tropical axes being mostly easterly and mid-latitude axes being mostly westerly. A separation using a threshold at zero nevertheless remains questionable, as there is still a sub-

stantial number of mid-latitude axes with easterly moisture transport. This happens most frequently around 60° latitude (Fig. 5c). From a synoptic perspective, this is most often associated with the cyclonic flow on the poleward side of a cyclone (example in Fig. 2b). A further problem with a cut-off at $0\,\mathrm{kg\,s^{-1}\,m^{-1}}$ eastward IVT is the frequent occurrence of mainly meridional moisture transport in the Southern Hemisphere (e.g., Fig. 2d), where slight variations off the meridional direction then determine whether an atmospheric river is detected.

Similar arguments hold for the poleward IVT (Fig. 5d). Here, the distribution is unimodal and centered close to zero poleward IVT, in particular with normalization. Consequently, almost as many axes exhibit equatorward and poleward moisture transport (equatorward transport in 44% of non-normalized transport axes and 40% of normalized axes). Further, the distributions of poleward IVT for tropical and extratropical transport axes show a large degree of overlap, such that poleward IVT does not seem to offer a suitable threshold to separate these two kinds of transport axes.

Despite mentioned differences between moisture transport axes and typical definitions of atmospheric rivers, these two concepts generally capture the same phenomenon in the mid-latitudes. For example, the occurrence of moisture transport axes along the North American west coast is often associated with strong precipitation (snapshot and composite analysis in Fig. 6) and the characteristic synoptic structure associated with atmospheric rivers in this region (as documented in Fig. 9 of Rutz et al., 2019) is very similar to the mean synoptic situation conditioned on the presence of a moisture transport axes in the same location (Fig. 6c,d).

7 Moisture transport axes in polar regions and their relation to warm moist intrusions

Moisture filaments and associated peaks in the moisture transport occur in a similar form also in polar regions (Woods et al., 2013). Gorodetskaya et al. (2014) discusses two cases where moisture filaments made landfall on the Antarctic coastline, referring to these features as *atmospheric rivers* to stress the similarities to their mid-latitude counterparts. The same phenomenon also regularly occurs in the Atlantic Arctic, but here they would typically be called *warm moist intrusions* (e.g., Woods & Caballero, 2016; Papritz et al., 2022). In the following, we relate detected moisture transport axes to both of these features.

Returning first to the Southern Ocean and the May-2009 case of Gorodetskaya et al. (2014), a moisture transport axis traces the essentially meridional moisture transport across all of the mid-latitudes from close to Madagascar onto the Antarctic continent (Fig. 7a,b). Their February-2011 case is similar in that it also features a well-defined moisture transport axis across all of the mid-latitudes, and is thus only shown in the supplement (Fig. A1c,d). In both cases, the moisture transport is well-captured without normalization. Normalized axes trace the moisture transport somewhat further into the continent (May-2009 case) or along the Antarctic coast line (February-2011 case).

The synoptic structure of the May-2009 case is typical for the region (Fig. 7c,d). A composite of all cases where moisture transport axes reach the Antarctic coastline within 200 km of the Gorodetskaya et al. (2014) case demonstrates a predominantly meridional orientation of the axes reaching the coastline (green contours in Fig. 7d). Few transport axes penetrate into the interior of the Antarctic continent; nearly all are diverted along the coastline (green contours and shading in Fig. 7d). In contrast, the composite moisture transport remains largely zonal throughout most of the mid-latitudes and only exhibits a cyclonic anomaly close to the Antarctic coast centered around 60°S (Fig. 7c).

An analogous composite analysis based on the occurrence of normalized transport axes yields a very similar synoptic structure (not shown). The composite, however, in-

cludes about six times more time steps than the composite shown in Fig. 7c,d. Therefore, the occurrence of a normalized transport axis should be regarded as an everyday weather event, whereas the non-normalized composite focuses on more pronounced—though still not unusual—events.

In the Atlantic Arctic, even more (non-normalized) transport axes occur within 200 km of Longyearbyen, Svalbard (compare Fig. 7c,d and Fig. 8c,d). In line with the findings of Serreze et al. (2015), this composite analysis highlights pronounced northeastward moisture transport from the mid-latitude North Atlantic (Fig. 8). Moisture transport axes occur frequently across the entire subpolar North Atlantic, between Greenland and Norway, with only a slight skew towards the Norwegian coast. The composite is also fully consistent with the case study discussed in Binder et al. (2017), with pronounced meridional moisture transport between France and Fram Strait (Fig. 8a,b).

These composites and synoptic examples suggest a good correspondence between our moisture transport axes and both polar atmospheric rivers and warm moist intrusions. To corroborate this finding, we systematically compare our transport axes with the occurrence of warm moist intrusions as defined by Woods et al. (2013). They define such intrusions by a transport threshold of $200\,\mathrm{Tg\,day^{-1}\,deg.\,long^{-1}}$ across 70°N, which corresponds to about $61\,\mathrm{kg\,s^{-1}\,m^{-1}}$. We relate this to the poleward IVT along all moisture transport axes detected between 68 and 72° latitude (Fig. 9c). We include detections within ±2° latitude to increase the sample size for this analysis.

About 40% of the normalized and 60% of non-normalized transport axes exceed this threshold (Fig. 9c). Further, a skew in the poleward IVT distribution towards positive values shows that moisture transport is predominantly poleward. The skew is particularly pronounced for non-normalized detections (red distribution in Fig. 9c). Nevertheless, about 20% of both normalized and non-normalized moisture transport axes around 70° latitude exceed a threshold of the opposite sign, signalling the regular occurrence of warm moist *extrusions* from the Arctic. This phenomenon has also been noticed by Papritz et al. (2022), who separated total and net moisture transport into the Arctic.

Such emphasized moisture export from the Arctic is plausible from the synoptic example in Fig. 2d. In this snapshot, a moisture transport axis turns equatorward around 60°S, tracing the warm front of a mature cyclone. An analogous synoptic situation with a cyclone core located in the Barents Sea would simultaneously yield strong moisture import into and export from the Arctic.

Besides their absolute number of occurrences, the main difference between normalized and non-normalized transport axes around 70°N is in the magnitude of the IVT (Fig. 9b). Few transport axes feature less than $200\,\mathrm{kg\,s^{-1}\,m^{-1}}$ without normalization, whereas the most frequently occurring IVT for the normalized axes is between 125 and $150\,\mathrm{kg\,s^{-1}\,m^{-1}}$. Analogous differences between the detections are evident for IWV, but here the shift in the most frequent value towards lower values for the normalized detections is somewhat less pronounced (Fig. 9a). While most polar transport axes feature IWV below $20\,\mathrm{kg\,m^{-2}}$, it is interesting to note the occasional occurrence of moisture transport axes with up to around $40\,\mathrm{kg\,m^{-2}}$ even at around 70° latitude (Fig. 9a).

8 Moisture transport axes in the Subtropics and Tropics

Moisture filaments from and towards the Subtropics have not yet been considered systematically. Many detection algorithms cut at 30° latitude or normalize the input fields to avoid detections in the subtropics (ARTMIP intercomparison; Rutz et al., 2019). Given that the Hadley circulation exhibits much less day-to-day variability than the extratropics, such that subtropical climate is generally well-described by monthly mean states (e.g., Vallis, 2006; Ogawa & Spengler, 2019), this disregard might be well justified. In contrast,

atmospheric rivers are considered a synoptic feature with a life cycle on the time scale of days. It is thus a priori unclear to what extent the atmospheric river concept remains physically meaningful at lower latitudes. Nevertheless, well-defined maxima in the moisture transport, i.e. moisture transport axes, do exist in the Subtropics and Tropics (cf., snapshot in Fig. 2g,h; climatologies in sec. 4 and Fig. 3).

The low-latitude case study and climatologies discussed previously suggest different dynamical reasons for the occurrence of moisture transport axes in this region. Some seem to capture seasonal circulation anomalies like the Indian Monsoon, some seem to be steered by orography (e.g., across the Maritime Continent and along the Andes), and some seem to capture actual intermittent moisture transport similar to that in the extratropics (e.g., Sahel region). The topographically steered moisture transport axes mostly vanish with normalization (Fig. 4), implying an almost continuous moisture transport in these regions. The Indian Monsoon remains visible with normalization by the annual means (Fig. 4), but does largely vanish when normalizing by the seasonal mean (not shown) due to the near-stationary flow during the monsoon season.

Using composite analysis, we contrast the moisture transport axes detected in the near-stationary Indian Monsoon with the intermittent transport axes detected over the Sahel region (Figs. 10, 11). The composite analysis for the Indian Monsoon is based on the occurrence of transport axes in the vicinity of Kolkata, India. For the non-normalized transport axes, the composite comprises 18 674 time steps, corresponding to about 55 days per year, highlighting the semi-permanent nature of the feature during the monsoon season (Fig. 10b). The composite moisture transport axes are diverted by the Himalayas, with westward-pointing moisture transport axes along the mountain range to the west of the Bay of Bengal, and eastward axes to the east (Fig. 10b). This diffluence is not visible in the direction of the mean transport (Fig. 10a), because the magnitude of the mean transport vector is relatively small along the Himalayas (gray contours in Fig. 10b). In combination with the high IWV evident in Fig. 10a, this indicates a variable transport direction along the mountain range.

For the Indian Monsoon, normalization reduces the number of detected events to about half (Fig. 10c,d). A moisture transport axis is thus present in the vicinity of Kolkata for about 30% of the time steps during the monsoon season. This frequency is similar to the peak occurrence of moisture transport axes in the North Atlantic, which just exceeds 25% during winter (Fig. 3a). Normalization thus isolates particularly pronounced moisture transport events within the otherwise relatively stationary monsoon circulation.

This conclusion is supported by the similar but clearer synoptic structure evident in the normalized composites (compare Fig. 10c,d with Fig. 10a,b). The atmosphere is even more loaded with water and precipitation is even more widespread (Fig. 10c). Further, the moisture transport features a closed cyclonic circulation over the Indian subcontinent (Fig. 10c). Upstream, a larger region exceeds an IVT of $300\,\mathrm{kg\,s^{-1}\,m^{-1}}$ (darkest gray contour in Fig. 10b,d), while fewer transport axes connect the Indian monsoon to the Somali Jet. This further indicates that the normalized composite emphasizes a regional/synoptic intensification of the Monsoon circulation over India.

With our second composite analysis, we move from one of the (seasonally) most humid to one of the most arid places in the Subtropics (Fig. 11). Here, the composites are based on the occurrence of moisture transport axes close to Timbuktu, Mali, which is located in the Sahel belt to the south of the Sahara Desert. The snapshot in Fig. 2g,h includes an example case included in this composite.

Both the composite based on normalized and non-normalized detections exhibit an extrusion from the Tropical belt of moisture associated with the ITCZ into the Sahel region (Fig. 11a,c). This extrusion is, however, much more pronounced in the nor-

malized composite (Fig. 11c) and features pronounced moisture transport across the Sahel and towards the northeast, crossing the Sahara into the Mediterranean. The tilted structure seen in the mean moisture transport is reflected in both normalized and non-normalized transport axis detections (Fig. 11b,d). Although the average precipitation along these transport axes not strong enough to exceed the contour level, the snapshot in Fig. 2g,h illustrates that scattered precipitation can be associated with such transport events.

In the Sahel region, the occurrence of moisture transport axes is very intermittent, mainly occurring during late summer (JAS) and winter to early spring (DJFMA). The non-normalized composite includes about 16 days per year and the normalized composite less than 2 days per year. Their occurrence during JAS coincides with the seasonal occurrence of African Easterly Waves (e.g., Berry et al., 2007). In contrast, the occurrence during winter and spring might be related to an influence from the mid-latitudes due to the southward displacement of the stormtrack (e.g., Spensberger & Spengler, 2020).

9 Summary and concluding remarks

We introduced a novel and generic feature detection algorithm for moisture filaments using an algorithm developed to detect upper tropospheric jets (Spensberger et al., 2017). We call the detected features *moisture transport axes* as these trace lines of maximum vertically integrated moisture transport (IVT). The name *moisture transport axes* and the visualization as lines are not meant to imply a continuous transport along the line. As Läderach and Sodemann (2016) and Dacre et al. (2019) pointed out, there is a continuous recycling of water along atmospheric rivers, even though some long-range transport of moisture does occur (Stohl et al., 2008; Sodemann & Stohl, 2013). Analogously, we expect the same to be true for moisture transport along our detected moisture transport axes.

In the mid-latitudes, moisture transport axes generally capture the same synoptic phenomenon as commonly used definitions of atmospheric rivers. Due to the structure-based definition of the feature, moisture transport axes often trace the moisture filament further into the subtropics, continents, or polar regions than typical definitions of atmospheric rivers, which usually cut at a fixed IWV and/or IVT threshold. Further, moisture transport axes reveal the substructure of atmospheric rivers with several distinct maxima in the IVT and they are not subject to any limitations in the orientation of the moisture transport.

For polar regions, we document a relation to warm moist intrusions and to existing polar adaptations of atmospheric rivers. Moisture transport axes thus highlight events with pronounced moisture import into polar regions. They, however, also reveal synoptic structures where much of the imported moisture is directly exported again. While such events are implicitly accounted for in the analysis of Papritz et al. (2022), the existence of such moisture export events is not obvious from previous studies on warm moist intrusions.

In the Tropics and Subtropics, moisture transport axes highlight both intermittent, seasonal and near-stationary features of the circulation. For example, moisture transport axes either highlight the continuously strong moisture transport in the Indian Monsoon circulation or the more transient peaks in the monsoon circulation, depending on the use of normalization. In the climatologically arid Sahel region, moisture transport axes reflect intermittent extrusions of moisture from the deep Tropics. Here, the normalization does not change the character of the detected event, but focuses the detections on much fewer, more pronounced events. Finally, moisture transport axes pick up the orographically steered South American low level jet as well as moisture transport along the straits of the Maritime continent. While these spotlights are far from providing a

comprehensive view of subtropical moisture transports, they clearly suggest that the concept of moisture transport axes remains meteorologically meaningful also in these regions.

In conclusion, our approach allows us to unify the concepts of atmospheric rivers and warm moist intrusions. As our definition is based on the elongated structure of moisture transport, our detection algorithm performs seamlessly from the Tropics across the mid-latitudes into the polar regions. The concept of transport axes might thus turn out to be particularly useful to study moist interactions between the Tropics and Subtropics, mid-latitudes, and polar regions. Our definition of moisture transport axes is likely also more robust across varying climates than commonly used definitions of atmospheric rivers, as our definition does not require changes to thresholds or a time-dependent normalization. Finally, following the approach of Spensberger and Spengler (2020), moisture transport axes enable the investigation of variability in the occurrence of atmospheric rivers largely independent from their varying intensity.

Appendix A Supplementary moisture transport axis snapshots

Open Research Section

The ERA5 reanalysis used in this study is publicly available. The jet detection algorithm is available as part of *dynlib*, a library of meteorological analysis tools (Spensberger, 2021).

Acknowledgments
We thank ECMWF for providing the ERA5 reanalysis used in this study. The reanalysis was obtained directly through the Meteorological Archival and Retrieval System (MARS).

References

Azad, R., & Sorteberg, A. (2017). Extreme daily precipitation in coastal western norway and the link to atmospheric rivers. *Journal of Geophysical Research: Atmospheres*, *122*(4), 2080-2095. doi: 10.1002/2016JD025615

Berry, G., Thorncroft, C., & Hewson, T. (2007, April). African easterly waves during 2004–analysis using objective techniques. *Monthly Weather Review*, *135*(4), 1251–1267. doi: 10.1175/MWR3343.1

Binder, H., Boettcher, M., Grams, C. M., Joos, H., Pfahl, S., & Wernli, H. (2017). Exceptional air mass transport and dynamical drivers of an extreme wintertime arctic warm event. *Geophysical Research Letters*, *44*(23), 12,028–12,036. doi: https://doi.org/10.1002/2017GL075841

Dacre, H. F., Clark, P. A., Martinez-Alvarado, O., Stringer, M. A., & Lavers, D. A. (2015). How do atmospheric rivers form? *Bulletin of the American Meteorological Society*, *96*(8), 1243–1255. doi: 10.1175/BAMS-D-14-00031.1

Dacre, H. F., Martínez-Alvarado, O., & Mbengue, C. O. (2019). Linking atmospheric rivers and warm conveyor belt airflows. *Journal of Hydrometeorology*, *20*(6), 1183–1196. doi: 10.1175/JHM-D-18-0175.1

Gorodetskaya, I. V., Tsukernik, M., Claes, K., Ralph, M. F., Neff, W. D., & Van Lipzig, N. P. M. (2014). The role of atmospheric rivers in anomalous snow accumulation in east antarctica. *Geophysical Research Letters*, *41*(17), 6199-6206. doi: 10.1002/2014GL060881

Griffith, H. V., Wade, A. J., Lavers, D. A., & Watts, G. (2020). Atmospheric river orientation determines flood occurrence. *Hydrological Processes*, *34*(23), 4547–4555. doi: 10.1002/hyp.13905

Hersbach, H., Bell, B., Berrisford, P., Hirahara, S., Horányi, A., Muñoz-Sabater, J., ... Thépaut, J.-N. (2020). The ERA5 global reanalysis. *Quarterly Journal of the Royal Meteorological Society*, *146*(730), 1999–2049. doi: 10.1002/qj.3803

Läderach, A., & Sodemann, H. (2016). A revised picture of the atmospheric moisture residence time. *Geophysical Research Letters*, *43*(2), 924–933. doi: 10.1002/2015GL067449

Lavers, D. A., Villarini, G., Allan, R. P., Wood, E. F., & Wade, A. J. (2012). The detection of atmospheric rivers in atmospheric reanalyses and their links to british winter floods and the large-scale climatic circulation. *Journal of Geophysical Research: Atmospheres*, *117*(D20). doi: 10.1029/2012JD018027

Lora, J. M., Shields, C. A., & Rutz, J. J. (2020). Consensus and disagreement in atmospheric river detection: Artmip global catalogues. *Geophysical Research Letters*, *47*(20), e2020GL089302. doi: 10.1029/2020GL089302

Montini, T. L., Jones, C., & Carvalho, L. M. V. (2019). The south american low-level jet: A new climatology, variability, and changes. *Journal of Geophysical Research: Atmospheres*, *124*(3), 1200–1218. doi: 10.1029/2018JD029634

Mundhenk, B. D., Barnes, E. A., & Maloney, E. D. (2016). All-season climatology and variability of atmospheric river frequencies over the north pacific. *Journal of Climate*, *29*(13), 4885–4903. doi: 10.1175/JCLI-D-15-0655.1

Newell, R. E., Newell, N. E., Zhu, Y., & Scott, C. (1992). Tropospheric rivers? – a pilot study. *Geophysical Research Letters*, *19*(24), 2401–2404. doi: 10.1029/92GL02916

Ogawa, F., & Spengler, T. (2019). Prevailing surface wind direction during air–sea heat exchange. *Journal of Climate*, *32*(17), 5601 - 5617. doi: 10.1175/JCLI-D-18-0752.1

Papritz, L., Hauswirth, D., & Hartmuth, K. (2022). Moisture origin, transport pathways, and driving processes of intense wintertime moisture transport into the arctic. *Weather and Climate Dynamics*, *3*(1), 1–20. doi: 10.5194/wcd-3-1-2022

Rutz, J. J., Shields, C. A., Lora, J. M., Payne, A. E., Guan, B., Ullrich, P., ... Viale, M. (2019). The atmospheric river tracking method intercomparison project (ARTMIP): Quantifying uncertainties in atmospheric river climatology. *Journal of Geophysical Research: Atmospheres*, *124*(24), 13777–13802. doi: 10.1029/2019JD030936

Serreze, M. C., Crawford, A. D., & Barrett, A. P. (2015). Extreme daily precipitation events at spitsbergen, an arctic island. *International Journal of Climatology*, *35*(15), 4574–4588. doi: https://doi.org/10.1002/joc.4308

Sodemann, H., & Stohl, A. (2013). Moisture origin and meridional transport in atmospheric rivers and their association with multiple cyclones. *Monthly Weather Review*, *141*(8), 2850–2868. doi: 10.1175/MWR-D-12-00256.1

Sorteberg, A., & Walsh, J. E. (2008). Seasonal cyclone variability at 70 °n and its impact on moisture transport into the arctic. *Tellus A: Dynamic Meteorology and Oceanography*, *60*(3), 570–586. doi: 10.1111/j.1600-0870.2007.00314.x

Spensberger, C. (2021, March). *Dynlib: A library of diagnostics, feature detection algorithms, plotting and convenience functions for dynamic meteorology.* Zenodo. Retrieved from `https://doi.org/10.5281/zenodo.4639624` (Dynlib has a development history of nearly a decade. During this time, numerous people have contributed to its development with code, bug fixes, bug reports and general feedback. Code contributions are generally acknowledged in the code and documentation of the respective functions. Here, I want to specifically acknowledge and thank for the contributions to the code from Chris Weijenborg, Clio Michel and Angus Munro. In addition I am grateful for reference implementations of the slope-related diagnostics by Lukas Papritz, and of line-feature detections by Gareth Berry, both of which served as a reference for the corresponding functions in dynlib. Dynlib is generally licensed under the CC-BY 4.0 as defined here, but some functions which were incorporated from other libraries are licensed under differing open-source licenses.) doi: 10.5281/zenodo.4639624

Spensberger, C., & Spengler, T. (2020). Feature-based jet variability in the upper troposphere. *Journal of Climate*, *33*(16), 6849–6871. doi: 10.1175/JCLI-D-19-0715.1

Spensberger, C., Spengler, T., & Li, C. (2017, June). Upper-tropospheric jet axis detection and application to the boreal winter 2013/14. *Monthly Weather Review*, *145*(6), 2363–2374. doi: 10.1175/mwr-d-16-0467.1

Stohl, A., Forster, C., & Sodemann, H. (2008). Remote sources of water vapor forming precipitation on the norwegian west coast at 60 °n–a tale of hurricanes and an atmospheric river. *Journal of Geophysical Research: Atmospheres*, *113*(D5). doi: 10.1029/2007JD009006

Vallis, G. K. (2006). *Atmospheric and oceanic fluid dynamics* (1st ed.). Cambridge University Press.

Viste, E., & Sorteberg, A. (2013). Moisture transport into the ethiopian highlands. *International Journal of Climatology*, *33*(1), 249–263. doi: 10.1002/joc.3409

Wick, G. A., Neiman, P. J., & Ralph, F. M. (2013). Description and validation of an automated objective technique for identification and characterization of the integrated water vapor signature of atmospheric rivers. *IEEE Transactions on Geoscience and Remote Sensing*, *51*(4), 2166–2176. doi: 10.1109/TGRS.2012.2211024

Woods, C., & Caballero, R. (2016, March). The role of moist intrusions in winter arctic warming and sea ice decline. *Journal of Climate*, *29*(12), 4473–4485. Retrieved from `https://doi.org/10.1175/JCLI-D-15-0773.1` doi: 10.1175/jcli-d-15-0773.1

Woods, C., Caballero, R., & Svensson, G. (2013). Large-scale circulation associated with moisture intrusions into the Arctic during winter. *Geophysical Research Letters*, *40*(17), 4717–4721. doi: 10.1002/grl.50912

Zhu, Y., & Newell, R. E. (1994). Atmospheric rivers and bombs. *Geophysical Research Letters*, *21*(18), 1999–2002. doi: 10.1029/94GL01710

Zhu, Y., & Newell, R. E. (1998). A proposed algorithm for moisture fluxes from atmospheric rivers. *Monthly Weather Review*, *126*(3), 725–735. doi: 10.1175/1520-0493(1998)126⟨0725:APAFMF⟩2.0.CO;2

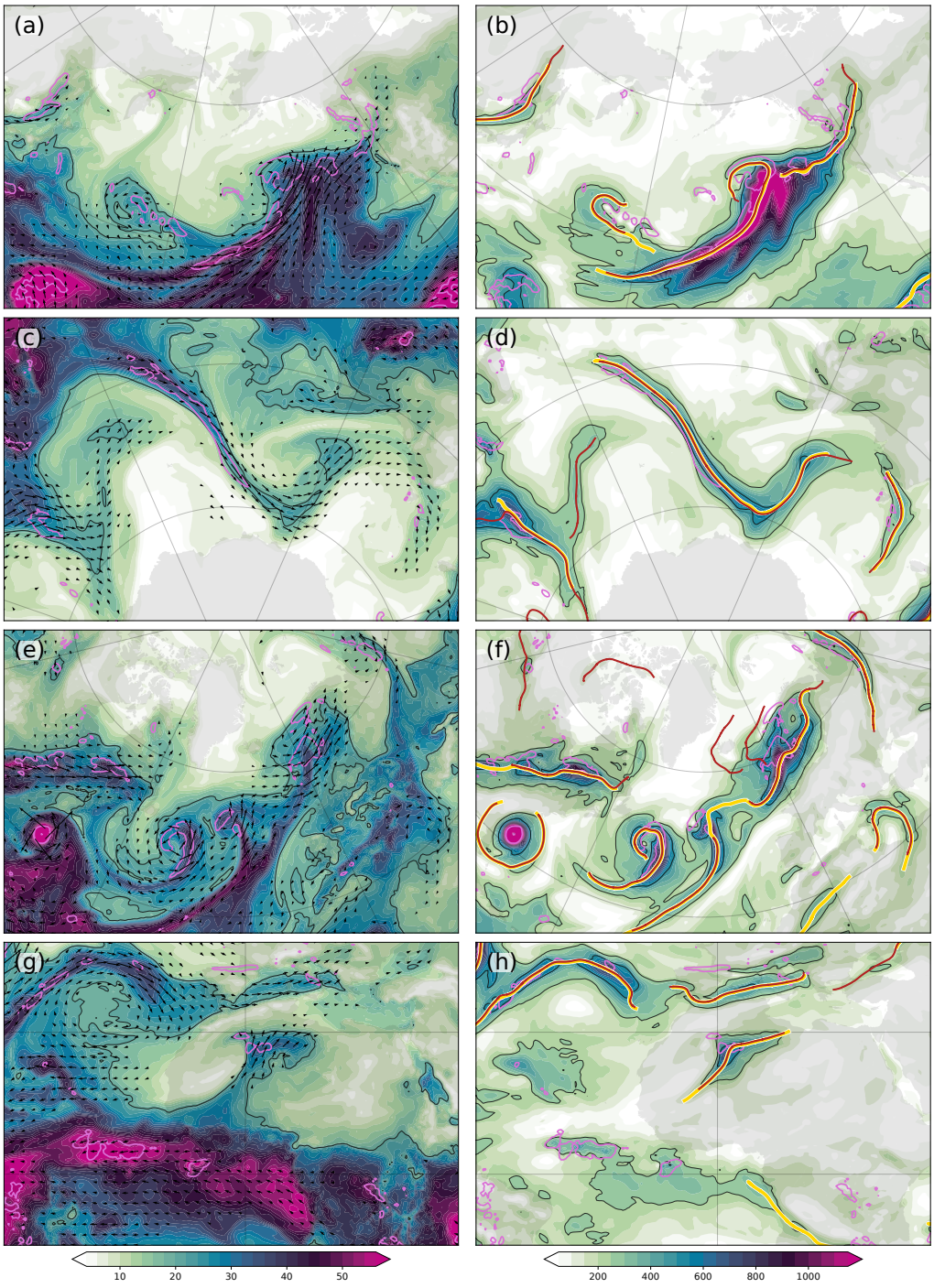

Figure 2. Snapshots of moisture transport axis occurrence. Panels (a-d) show atmospheric river cases discussed by Lora et al. (2020) by 5 November 2006, 09Z, and 14 November 2006, 09Z, respectively, (e,f) the strongest river case listed in Azad and Sorteberg (2017) on 14 September 2005, 00Z, and (g,h) a moisture transport axis over the Saharan Desert on 15 December 2017, 06 UTC. The left column shows total column water vapor [kg/m^2] (shading), IVT (arrows), and total precipitation (pink contour, 1 mm/h). The gray contour highlights the 20 mm total column water vapor contour. The right column shows the magnitude of IVT [kg m/s]. Precipitation is shown as in the left column and gray contours mark the 250 and 500 kg m/s contours of the water vapor transport. Finally, the yellow and red lines show detected moisture transport axes and normalized moisture transport axes, respectively.

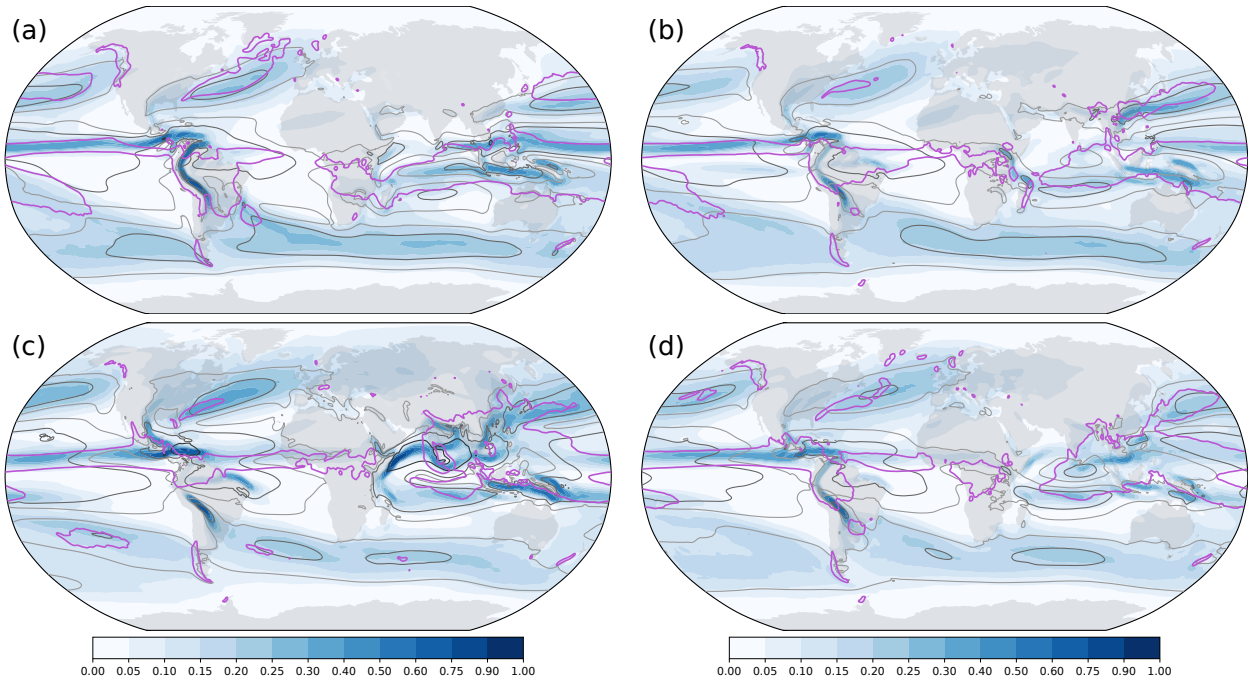

Figure 3. Climatological occurrence of moisture transport axes within 200 km of any given location for (a) DJF, (b) MAM, (c) JJA, and (d) SON. Grey contours show the climatological magnitude of the vertically integrated water vapor transport with contours at 100, 200, and 400 kg /(m s) and the pink contour marks the region exceeding 5 mm/day of total precipitation.

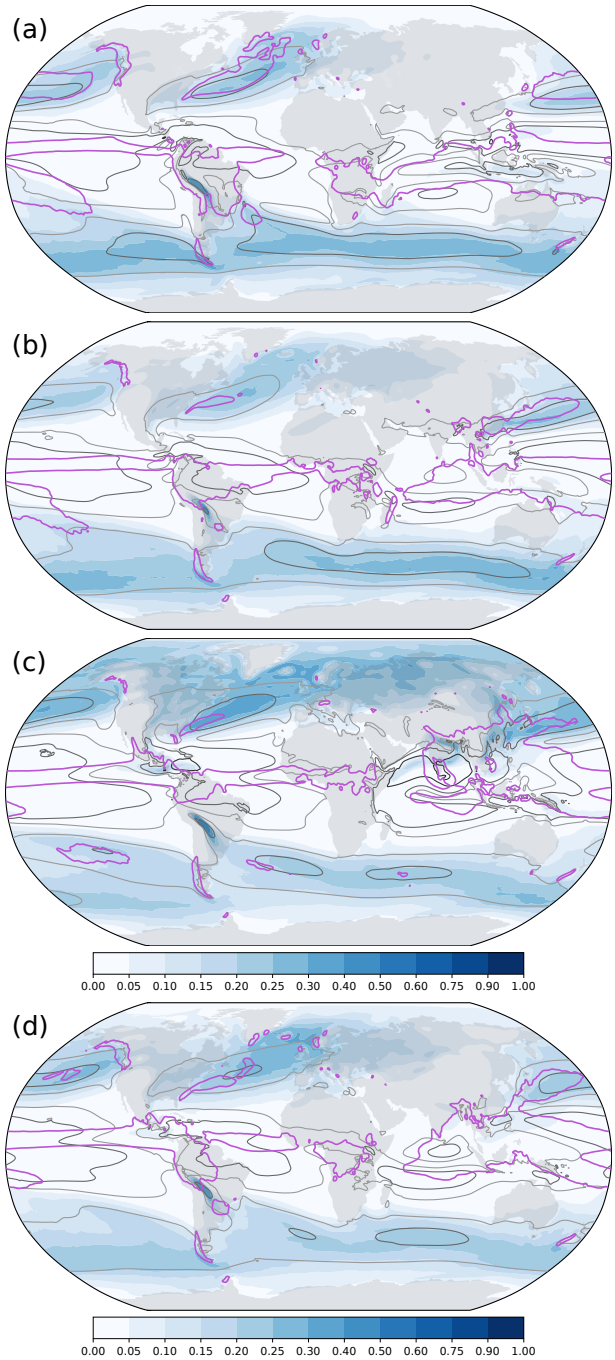

Figure 4. As Fig. 3, but for the normalized moisture transport axes.

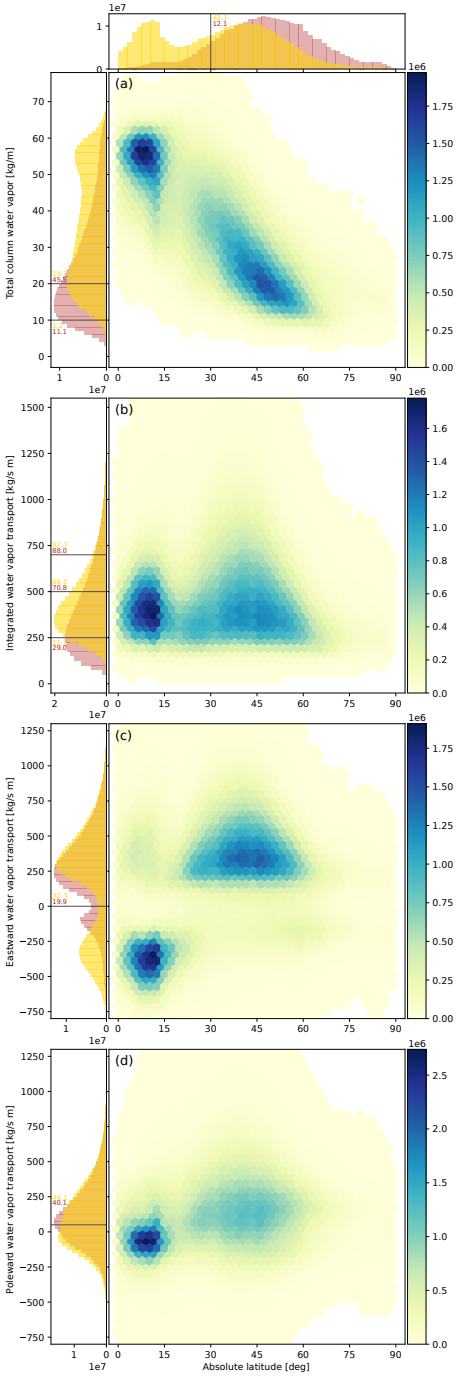

Figure 5. Two-dimensional histograms showing the occurrence counts of non-normalized moisture transport axes in phase spaces defined by latitude and (a) total column water vapor and (b) magnitude of IVT, as well as (c) eastward and (d) poleward component of IVT. One-dimensional histograms along the respective axes are displayed in yellow along the sides. Red histograms in these side panels show the occurrence of normalized moisture transport axes. Typical detection thresholds used for atmospheric river detections are indicated by lines across the one-dimensional histograms, with the adjacent numbers indicating the percentile at which these lines occur in the respective distributions.

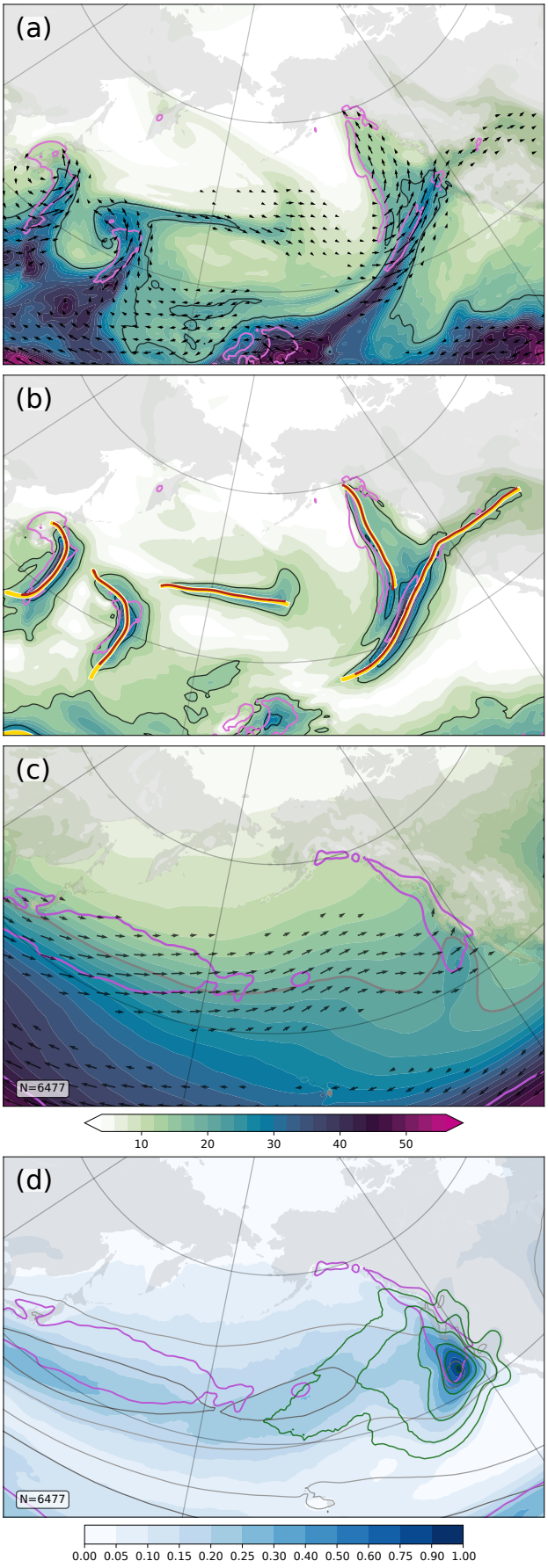

Figure 6. (a,b) Snapshot of a atmospheric river case from 15 February 2014, 09Z, discussed in Rutz et al. (2019) analogous to each row in Fig. 2. (c,d) Composites based on the occurrence of a normalized moisture transport axis within 200 km of the position 39°N, 124°W (cf. Fig. 9 of Rutz et al., 2019). (c) Total column water vapor [kg/m^2] (shading) with the gray contour highlighting the 20 kg/m^2 contour, and IVT (arrows), and total precipitation (pink contour at 5mm/day). (d) Frequency of occurrence of normalized moisture transport axes within 200 km. Dark green contours show the frequency of occurrence for only those moisture transport axes

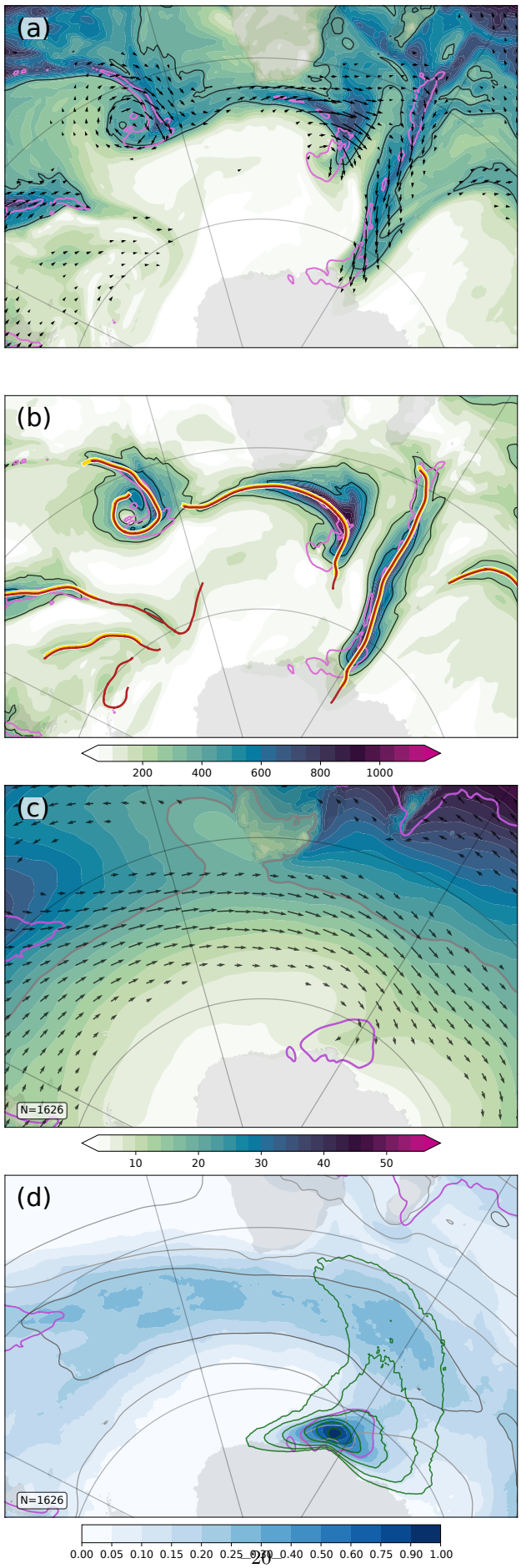

Figure 7. As Fig. 6, but for atmospheric rivers making landfall on Antarctica. The snapshot from 19 May 2009, 00Z in (a,b) is one of the cases discussed in Gorodetskaya et al. (2014). The composite (c,d) is based on moisture transport axes occurring within 200 km of the landfall location.

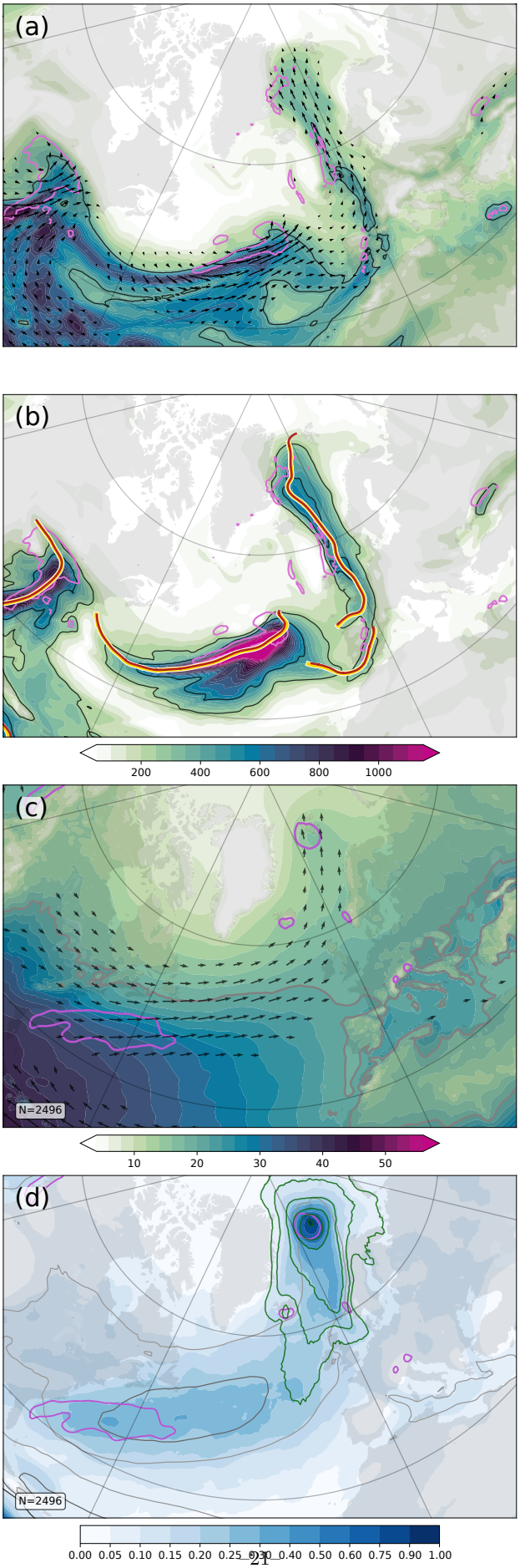

Figure 8. As Fig. 6, but for moisture transport axes around Svalbard. The snapshot from 29 December 2015, 00Z, in (a,b) is discussed in Binder et al. (2017). The composite (c,d) is based on moisture transport axes occurring within 200 km of Longyearbyen, Svalbard.

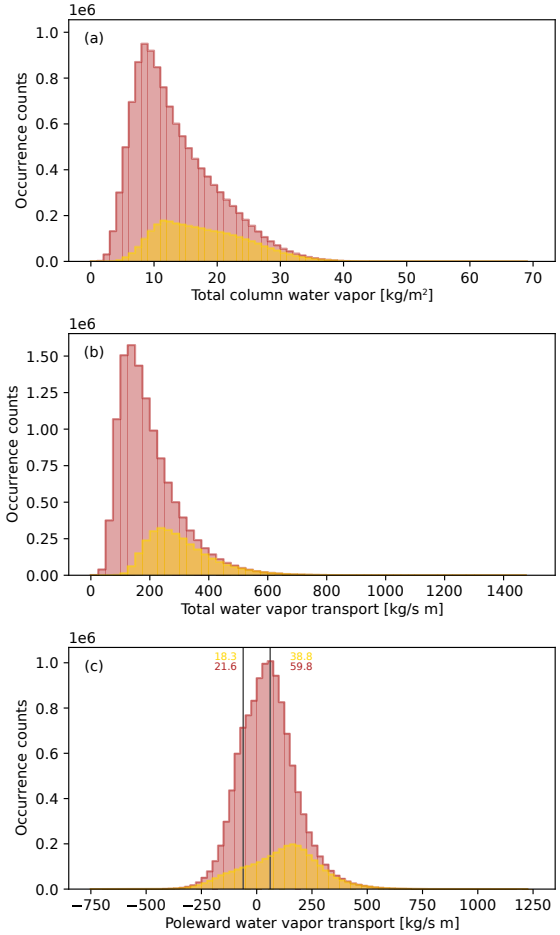

Figure 9. As the one-dimensional histograms on the left-hand side of Fig. 5a,b and d, but based on moisture transport axes detected within 68-72°N/S. As in Fig. 5, yellow and red histograms represent non-normalized and normalized detections, respectively. For the relevance of the vertical lines and percentiles in (c) refer to the main text.

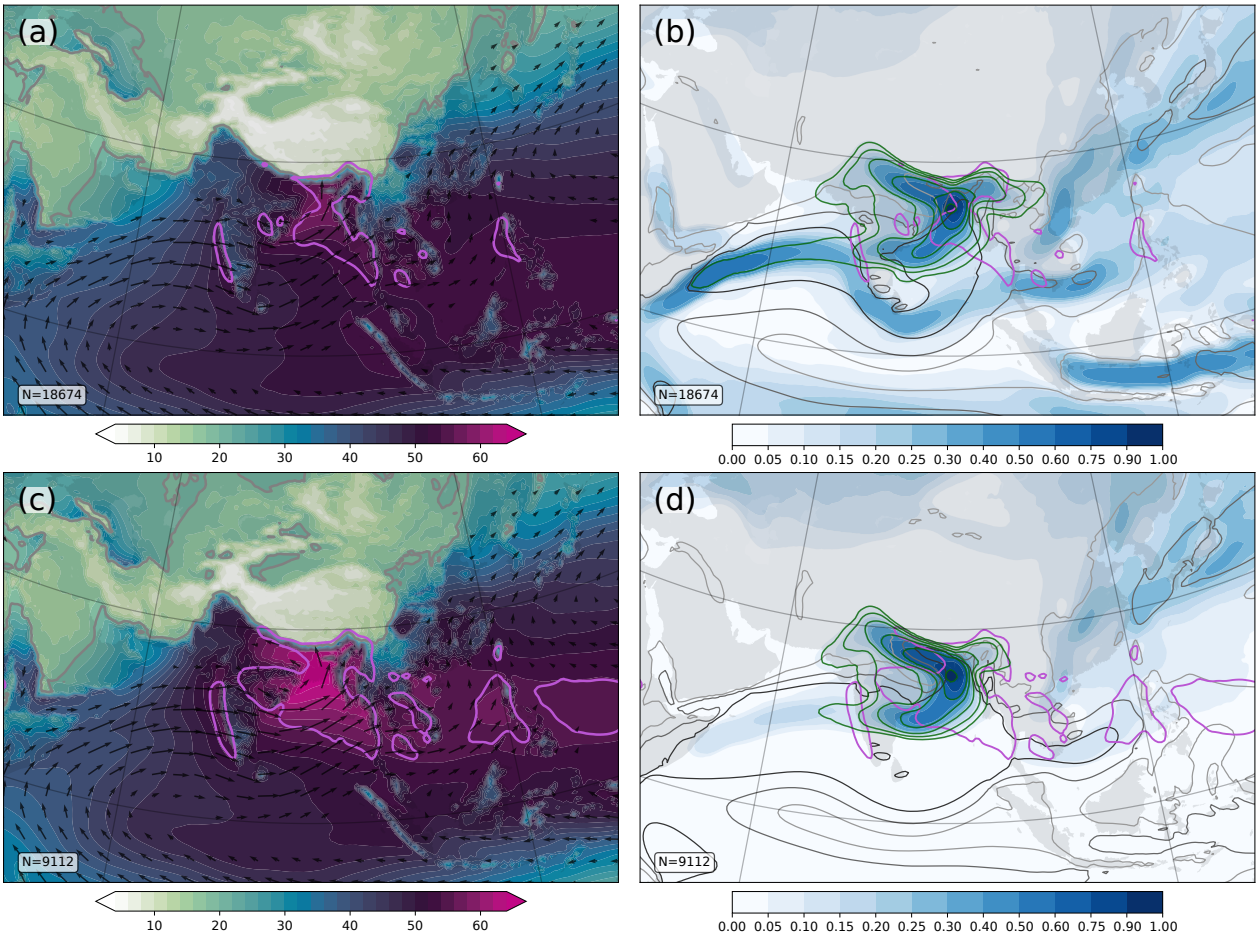

Figure 10. Each row as the composites in Fig. 6c,d, but for (a,b) moisture transport axes within 200 km of Kolkata, India, and (c,d) normalized moisture transport axes around the same location.

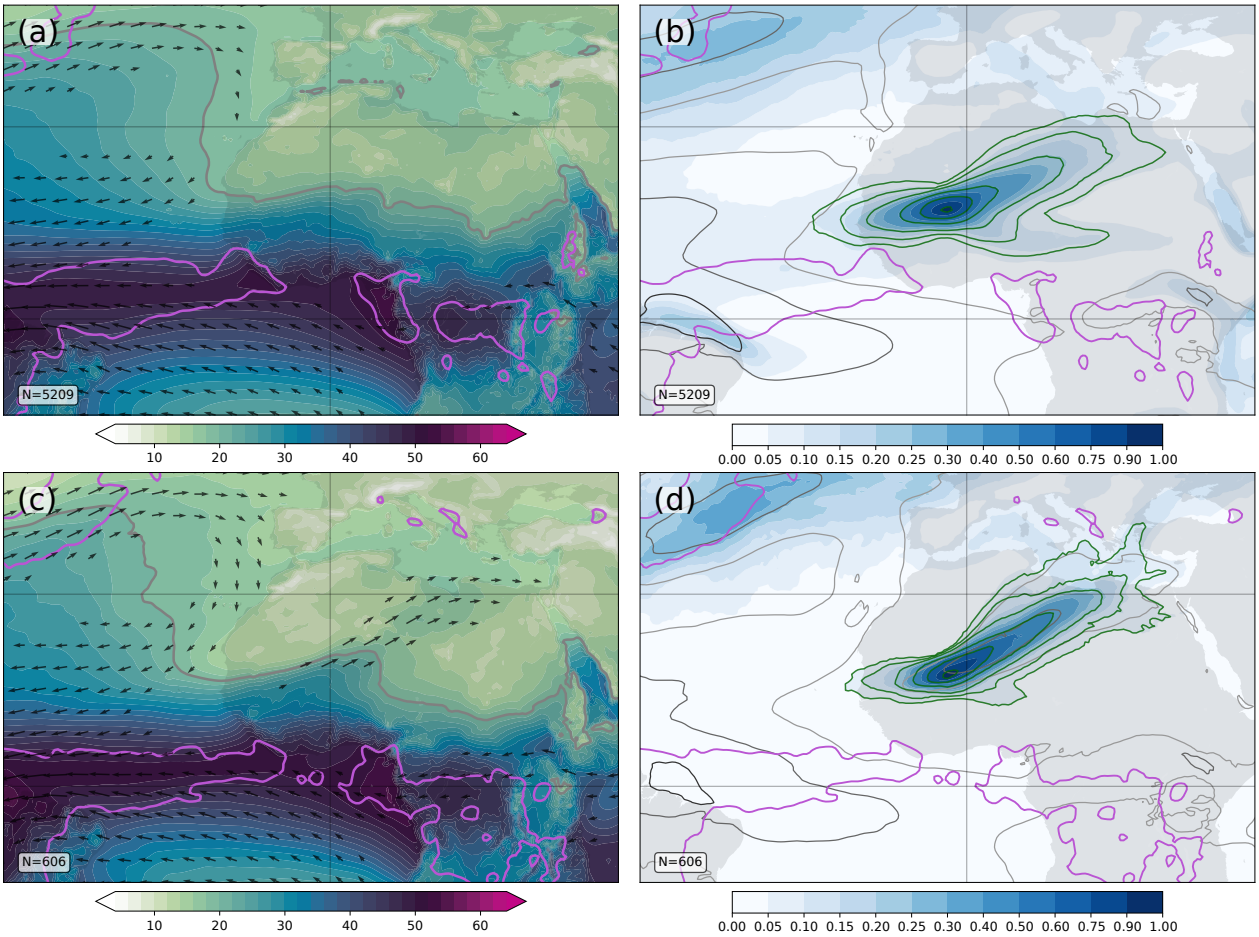

Figure 11. Each row as the composites in Fig. 6c,d, but for (a,b) moisture transport axes within 200 km of Timbuktu, Mali, in the Sahel region, and (c,d) normalized moisture transport axes around the same location.

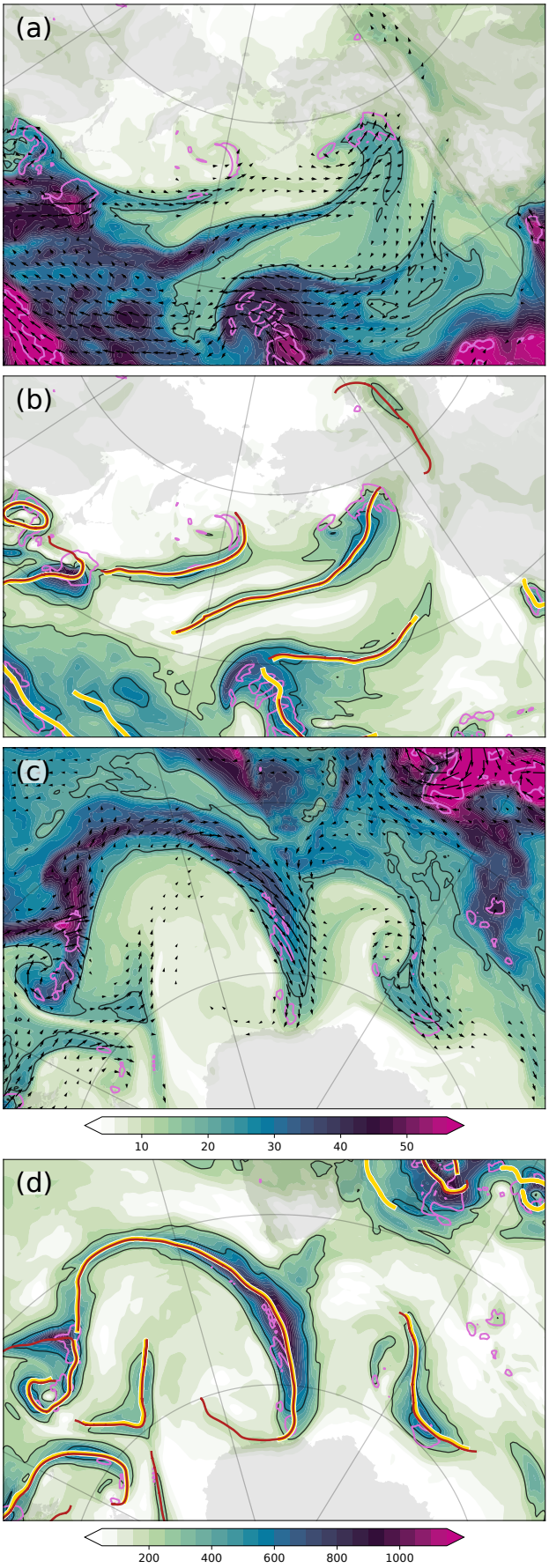

Figure A1. As Fig. 2, but (a,b) for the other atmospheric river case discussed in Rutz et al. (2019), and (c,d) the other atmospheric river case discussed in Gorodetskaya et al. (2014). The rows show (a,b) 23 October 2006, 12Z, and (c,d) 15 February 2011, 00Z.